

Photocatalytic reduction of CO<sub>2</sub> over a hybrid photocatalyst composed of WO<sub>3</sub> and graphitic carbon nitride (g-C<sub>3</sub>N<sub>4</sub>) under visible light

Teruhisa Ohno<sup>a,b,c,\*</sup>, Naoya Murakami<sup>a,c</sup>, Takahiro Koyanagi<sup>a</sup>, Yin Yang<sup>a</sup>

<sup>a</sup> Department of Materials Science, Faculty of Engineering, Kyushu Institute of Technology, 1-1 Sensuicho, Tobata, Kitakyushu 804-8550, Japan

<sup>b</sup> JST, PRESTO, 4-1-8 Honcho Kawaguchi, Saitama 332-0012, Japan

<sup>c</sup> JST, ACT-C, 4-1-8 Honcho Kawaguchi, Saitama 332-0012, Japan

\* Corresponding author. Tel.: +81 93 884 3318; fax: +81 93 884 3318.

E-mail address: tohno@che.kyutech.ac.jp (T. Ohno).

## Abstract

Graphitic carbon nitride (g-C<sub>3</sub>N<sub>4</sub>) has attracted much attention as a metal-free semiconductor having visible light absorption and relatively high chemical stability. g-C<sub>3</sub>N<sub>4</sub> can reduce CO<sub>2</sub> to organic fuels such as methanol (CH<sub>3</sub>OH), formic acid (HCO<sub>2</sub>H), and methane (CH<sub>4</sub>) under visible light irradiation. However, oxidation potential of g-C<sub>3</sub>N<sub>4</sub> is not enough for water oxidation. Therefore, we focused on hybridization of g-C<sub>3</sub>N<sub>4</sub> and tungsten(VI) oxide (WO<sub>3</sub>) which has high oxidation potential for water oxidation. In this study, we examined CO<sub>2</sub> reduction by composite photocatalyst of g-C<sub>3</sub>N<sub>4</sub> and WO<sub>3</sub>, which was prepared by three methods (mixture using an agate mortar, impregnation and planetary mill). As a result, composite photocatalyst prepared with planetary mill showed the highest photocatalytic activity.

Photodeposition of silver or gold nanoparticles only on g-C<sub>3</sub>N<sub>4</sub> of the hybrid photocatalyst induced an increase in CH<sub>3</sub>OH because the loaded metal nanoparticles play an important role in multi-electron reduction of CO<sub>2</sub>. Photocatalytic activity of the Au-loaded hybrid photocatalyst composed of g-C<sub>3</sub>N<sub>4</sub> and WO<sub>3</sub> was 1.7-times higher than that of the hybrid photocatalyst without Au loading.

In addition, we investigated photocatalytic reaction mechanism of composite photocatalyst by double-beam photoacoustic spectroscopy. This result revealed Z-scheme reaction proceed in the composite photocatalyst to maintain high oxidation ability of WO<sub>3</sub> and high reduction ability of g-C<sub>3</sub>N<sub>4</sub>, resulting in high photocatalytic activity.

Keywords: Hybrid photocatalyst; Graphitic carbon nitride; Tungsten oxide; Reduction of Carbon Dioxide; Z-scheme reaction

## 1. Introduction

Carbon dioxide (CO<sub>2</sub>) is one of the major compounds responsible for global warming, which has now become a global environmental issue because fossil fuel consumption will cause a monotonical increase in the atmospheric CO<sub>2</sub> concentration in the future [1]. Therefore, CO<sub>2</sub> conversion or energy-oriented use is a priority subject of investigation throughout the world. Effective utilization of clean and abundant solar energy for CO<sub>2</sub> conversion will be a promising solution not only for energy issues due to the consumption of natural energy sources but also for many problems caused by greenhouse gases [2]. In order to efficiently utilize solar energy, photocatalytic CO<sub>2</sub> reduction to produce useful fuels under visible light, mimicking artificial

photosynthesis, is one possible solution. Actually, photocatalytic reaction over semiconductor photocatalysts has the potential to reduce CO<sub>2</sub> into hydrocarbons using water as an electron donor. For instance, Inoue and coworkers first reported photocatalytic CO<sub>2</sub> reduction in a semiconductor aqueous suspension to produce hydrocarbon fuels such as formaldehyde (HCHO), formic acid (HCOOH), methanol (CH<sub>3</sub>OH), and methane (CH<sub>4</sub>) [3]. In addition, metal oxide semiconductor photocatalysts including titanium(IV) oxide (TiO<sub>2</sub>) can produce formic acid (HCOOH), formaldehyde (HCHO), methanol (CH<sub>3</sub>OH), and methane (CH<sub>4</sub>) [3-16]. However, quantum yields for photocatalytic CO<sub>2</sub> reduction have been low. The carbon source of the products is not clear. However, most of the photocatalytic CO<sub>2</sub> reductions using metal oxide semiconductor photocatalysts are carried out under UV-light irradiation, and the synthetic process and recipe of the photocatalysts are complicated. Therefore, visible-light-driven materials with high efficiency and stability represent a central challenge in the field of photocatalytic CO<sub>2</sub> conversion for energy-oriented use.

Recently, a visible light-responsive graphitic carbon nitride (g-C<sub>3</sub>N<sub>4</sub>) photocatalyst with high reduction ability was attracted much attention since hydrogen evolution over g-C<sub>3</sub>N<sub>4</sub> had reported to proceed from water under visible-light irradiation in the presence of sacrificial reagents [17]. Since Wang and co-workers first reported polymeric graphitic carbon nitride (g-C<sub>3</sub>N<sub>4</sub>) as a novel photocatalyst that exhibited photoactivity for H<sub>2</sub> production under visible-light irradiation, [18] many efforts have been made to synthesize g-C<sub>3</sub>N<sub>4</sub> through thermal treatment of some nitrogen-rich organic precursors, such as cyanamid, dicyanamide, triazine and heptazine derivatives [19-26]. Band gap and flat-band potential of g-C<sub>3</sub>N<sub>4</sub> were reported to be 2.67 eV and -1.42 V, respectively (versus Ag/AgCl, pH 6.6) [27]. Although, oxidation ability of g-C<sub>3</sub>N<sub>4</sub> is low enough for efficient oxidation of water, it has high reduction ability because of the high conduction band potential. Moreover, g-C<sub>3</sub>N<sub>4</sub> can be synthesized by a simple and low-cost route, and it has relatively high stability under light irradiation in water solution as well as in acid or base solutions due to the strong covalent bonds between carbon and nitride atoms [28]. g-C<sub>3</sub>N<sub>4</sub> photocatalysts are mainly applied to pollutant degradation or H<sub>2</sub> production, and there are only a few reports on the application to photocatalytic CO<sub>2</sub> reduction. Very recently, Dong and coworkers reported that g-C<sub>3</sub>N<sub>4</sub> can reduce CO<sub>2</sub> to CO in the presence of water vapor under visible-light irradiation [29]. In addition, Mao et al. directly heated urea or melamine to produce two kinds of g-C<sub>3</sub>N<sub>4</sub> photocatalysts that can reduce CO<sub>2</sub> to methanol and ethanol.[30] However, as mentioned above, the photocatalytic activity of g-C<sub>3</sub>N<sub>4</sub> for CO<sub>2</sub> reduction is relatively low in most cases because of low efficiency of the counter reaction, which is oxidation of water. In order to overcome this problem, we focused on a hybrid of two semiconductors to improve photocatalytic activity for CO<sub>2</sub> reduction under visible-light irradiation. Some studies have suggested that a charge transfer with charge separation model [31-34] or

Z-scheme model [18, 35, 36] proceeds at the interface between two kinds of semiconductors in a hybrid photocatalyst, resulting in an increase in photocatalytic activity.

In this study, we hybridized g-C<sub>3</sub>N<sub>4</sub> with WO<sub>3</sub>, which are specialized for reduction of CO<sub>2</sub> and for oxidation of water, respectively. WO<sub>3</sub> is known to exhibit visible-light absorption and show photocatalytic activity for oxidation of organic compounds or water under visible light.[37-39] Recently, there have been several reports on hybrids of g-C<sub>3</sub>N<sub>4</sub> with TiO<sub>2</sub> [40], TaON [41], and poly(3-hexylthiophene) [42]. However, a charge separation mechanism was employed in these photocatalysts and explanation of the mechanism was not sufficient. In the present study, we also elucidated the reaction mechanism of the hybrid photocatalyst using DB-PAS measurement.

## 2 Experimental Sections

### 2.1. Materials

g-C<sub>3</sub>N<sub>4</sub> powders were prepared by heat treatment of melamine (Wako Pure Chemical Industries, Ltd., 99%). Thirty grams of melamine in an alumina pot was heated at 550 °C for 4 h with a temperature rising rate of ca. 9 °C min<sup>-1</sup> in a muffle furnace [43]. WO<sub>3</sub>, silver nitrate, deuterium oxide, and chloroauric acid were purchased from Wako Pure Chemical Industries, Ltd. <sup>13</sup>CH<sub>3</sub>OH was obtained from ISOTECH. Other chemicals were obtained from commercial sources as guaranteed reagents and were used without further purification.

### 2.2. Preparation of hybrid photocatalysts

g-C<sub>3</sub>N<sub>4</sub> and WO<sub>3</sub> were hybridized in appropriate ratios between 100 : 0 – 0 : 100 (wt : wt) by a planetary mill method. The samples which were prepared in g-C<sub>3</sub>N<sub>4</sub> and WO<sub>3</sub> at the ratio of 1:2, 1:1 and 2:1 with a planetary mill, were referred to GW12, GW11 and GW21, respectively. Hybrid photocatalysts of WO<sub>3</sub> and g-C<sub>3</sub>N<sub>4</sub> at the ratio of 1:1 were also prepared by an agate mortar method and sonication method. For the agate mortar method, two kinds of powders were ground by an agate mortar for ca. 20 min. For the sonication method, two kinds of powders were suspended in 20 ml of ion-exchanged water by sonication for 30 min and subsequently stirred for 3 h. Then the sample was separated by filtration, washed with ion-exchanged water several times, and dried in a vacuum drying oven at 60 °C overnight. For the planetary mill method, 1.5 g of each kind of powders and 20 ml of ion-exchanged water were added to a 50 mL agate bowl containing 50 g of yttrium-stabilized zirconia grinding beads (NIKKATO Co. Ltd., Φ = 0.6 mm). Then the bowl was placed on a planetary mill (Fritsch Japan Co. Ltd., Planetary Micro Mill pulverisette 7) and the planetary mill was operated at 750 rpm for 10 min. After removing the beads by screening, the

sample was separated by filtration, washed with ion-exchanged water several times, and dried in a vacuum drying oven at 60 °C overnight. Denotation of samples names and the hybrid methods are summarized in Table 1.

Table 1 Abbreviations and  $S_{\text{BET}}$  of Hybrid photocatalyst prepared by three kinds of process and their original compound.

	Sample	Treatment	$S_{\text{BET}} / \text{m}^2 \text{g}^{-1}$
g-C <sub>3</sub> N <sub>4</sub>	g-C <sub>3</sub> N <sub>4</sub>	No treatment	10
WO <sub>3</sub>	WO <sub>3</sub>	No treatment	7
p-g-C <sub>3</sub> N <sub>4</sub>	Milled g-C <sub>3</sub> N <sub>4</sub>	Planetary mill	21
p-WO <sub>3</sub>	Milled WO <sub>3</sub>	No treatment	10
a-CW	g-C <sub>3</sub> N <sub>4</sub> , WO <sub>3</sub>	Agate mortar	8
s-CW	g-C <sub>3</sub> N <sub>4</sub> , WO <sub>3</sub>	Sonication	8
p-CW	g-C <sub>3</sub> N <sub>4</sub> , WO <sub>3</sub>	Planetary mill	17

### 2.3. Au or Ag co-catalyst-loaded hybrid photocatalysts (co-catalysts mainly deposited on g-C<sub>3</sub>N<sub>4</sub>)

For preparation of Au loaded hybrid photocatalysts, we used a photodeposition method as follows. Firstly, a hydrogen tetrachloroaurate(III) was dissolved in 50 ml of iron-exchange water. Secondly, g-C<sub>3</sub>N<sub>4</sub> particles (500 mg) were suspended in 50 mL of an ethanol aqueous solution (10 vol %) containing an appropriate amount Au precursor and the solution was applied ultrasonic treatment for 10 minutes. After N<sub>2</sub> bubbling for 30 minutes, an aqueous suspension was irradiated by using light-emitting diode (Nichia, NCCU033) at a wavelength of ca. 365 nm and an intensity of 0.3 mW cm<sup>-2</sup> for 24 h with vigorous magnetic stirring. For photodeposition of Ag, an aqueous suspension consisting of g-C<sub>3</sub>N<sub>4</sub> particles (500 mg) and 50 mL of ion-exchanged water containing an appropriate amount of silver nitrate was photoirradiated under the same conditions. After irradiation, photodeposited samples were obtained by filtration, washing with ion-exchanged water several times, and drying in a vacuum drying oven at 60 °C overnight. The net amounts of Au and Ag compounds on the surface of g-C<sub>3</sub>N<sub>4</sub> were estimated by analysis of the filtrate with inductively coupled plasma optical emission spectroscopy (ICPOES; Shimadzu, ICPS-8000). ICP analysis revealed that the net molar amounts of Au and Ag compounds photodeposited on g-C<sub>3</sub>N<sub>4</sub> were more than 99% of the provided molar amounts of Au and Ag. Co-catalyst-loaded hybrid photocatalysts composed of WO<sub>3</sub> and Au or Ag-loaded g-C<sub>3</sub>N<sub>4</sub> at the ratio of 2:1 were also prepared by the planetary mill.

#### 2.4. Characterization of prepared samples

Crystal structures of the particles were confirmed by using an X-ray diffractometer (Rigaku, MiniFlex II) with Cu K $\alpha$  radiation ( $\lambda = 1.5405 \text{ \AA}$ ). A diffuse reflectance spectrum was measured using a UV-visible spectrophotometer (Shimadzu, UV-2550 and 2600) equipped with an integrating sphere unit (ISR-240A and ISR-2600plus). The specific surface areas ( $S_{\text{BET}}$ ) of the particles were measured by nitrogen adsorption on the basis of the Brunauer–Emmett–Teller equation with a surface area analyzer (Quantachrome, Nova 4200e). The morphology of prepared particles was observed by scanning electron microscopy (SEM; JEOL, JSM-6701FONO) and transmission electron microscopy (TEM; Hitachi, H-9000NAR). The net amounts of Au or Ag compounds on the hybrid photocatalysts were estimated by analysis of the filtrate with inductively coupled plasma optical emission spectroscopy (ICP-OES; Shimadzu, ICPS-8000).

#### 2.5. Photocatalytic reduction of CO<sub>2</sub>

Before evaluation of the photocatalytic activity, each sample was irradiated with UV light using black light (UVP, XX-15BLB) for 24 h in order to remove organic compounds on the sample. Photocatalytic reduction of CO<sub>2</sub> was carried out under ambient pressure (1 atm) at 297 K. A light-emitting diode (LED; Epitex, 30M32L), which emitted light at a wavelength of ca. 435 nm and an intensity of 3.0 mW cm<sup>-2</sup>, was used as the light source for photocatalytic evaluation, and a test tube containing 3 mg of the hybrid photocatalyst and 5 mL ion-exchanged water saturated with CO<sub>2</sub> was photoirradiated with stirring for 24 h. For the labeling experiment, <sup>13</sup>CO<sub>2</sub> was used instead of <sup>12</sup>CO<sub>2</sub>. Other experimental conditions were exactly the same as those for <sup>12</sup>CO<sub>2</sub> photocatalytic reduction experiments.

Reaction products in liquid and gas phases were analyzed by gas chromatography (Hitachi G-3500, FID detector) with DB-WAXETR columns, gas chromatography (GL Science 490-GC, micro TCD detector) with MS-5A columns, and ion chromatography (Dionex, ICS-900) with IonPac AS-12A columns. Apparent quantum efficiency (QE) was defined by the following equation because of a 6-hole process for production of CH<sub>3</sub>OH as a main product from CO<sub>2</sub> reduction.

$$\begin{aligned} \text{QE} &= \frac{\text{Number of reacted electrons}}{\text{Number of incident photons}} \times 100 \\ &= \frac{\text{Number of generated CH}_3\text{OH molecules} \times 6}{\text{Number of incident photons}} \times 100 \end{aligned}$$

#### 2.6. DB-PA spectroscopic measurement

A gas-exchangeable photoacoustic (PA) cell equipped with two valves for gas flow was used, and a sample was placed in the cell. The atmosphere was controlled by a flow of artificial O<sub>2</sub> and N<sub>2</sub> containing ethanol vapor (mixture of N<sub>2</sub> and O<sub>2</sub> gas + EtOH), and the measurements were conducted after shutting off the valves, i.e., in a closed system at room temperature. An LED emitting light at ca. 625 nm (Lumileds, Luxeon LXHL-ND98) was used as a probe light, and the output intensity was modulated by a digital function generator (NF, DF1905) at 80 Hz. In addition to the modulated light, a blue LED (Lumileds, Luxeon LXHL-NB98, emitting light at ca. 435 nm, 0.5 mW cm<sup>-2</sup>) was also used as simultaneous continuous irradiation for photoexcitation. The PA signal acquired by a condenser microphone buried in the cell was amplified and monitored by a digital lock-in amplifier (NF, LI5640). Detailed setups of DB-PA spectroscopic measurements have been reported previously [44].

### 2.7 . Labeling experiments using <sup>13</sup>CO<sub>2</sub> reduction of CO<sub>2</sub>

Before evaluation of the photocatalytic activity, each sample was irradiated with UV light using black light (UVP, XX-15BLB) for 1 day in order to remove organic compounds on the sample. (Light intensity)

Degas and purge <sup>13</sup>CO<sub>2</sub> processes was shown Fig. S1. Photocatalysts powder 3 mg were ultrasonically dispersed in deionized water (5 mL). After complete degassing the whole system by diaphragm pump (Process 1), <sup>13</sup>CO<sub>2</sub> gas was bubbling for 15 min (Process 2). CO<sub>2</sub> photoreduction is performed for 24 h during LED irradiation (Process 3). After the reaction, the photocatalysts was removed by centrifugal separation. The aqueous samples (4 ml) for <sup>1</sup>H-NMR are dissolved in D<sub>2</sub>O (1 ml). 3-(Trimethylsilyl)-1-propanesulfonic acid sodium salt (SIGMA-ALDRICH) was used as an internal standard compound.

## 3 Results and Discussion

### 3.1. Characterization

Figure 1 shows diffuse reflectance spectrum of milled g-C<sub>3</sub>N<sub>4</sub>, milled WO<sub>3</sub> and the hybrid photocatalyst composed of g-C<sub>3</sub>N<sub>4</sub> and WO<sub>3</sub> at the ratio of 1 : 1 (p-CW). These photocatalysts exhibited visible-light absorption, and their absorption edges were around 500 nm.

The XRD pattern (Fig. 2) for g-C<sub>3</sub>N<sub>4</sub> showed its graphite stacking structures. The two diffraction peaks at 2θ = 13.1° and 27.4° match well with the (100) and (002) crystal planes of layered g-C<sub>3</sub>N<sub>4</sub>[18]. The strong diffraction peak at 2θ = 27.4° is a characteristic indicator of layered stacking with a distance of 0.326 nm, and the in-planar repeating tri-s-triazine unit with a

period of 0.675 nm can be clearly observed from the diffraction peak at  $2\theta=13.1^\circ$ , which is consistent with the reported results for g-C<sub>3</sub>N<sub>4</sub>[45]. The average crystal size was calculated by using Scherrer's formula to be 8.8 nm, according to the (002) peaks in the XRD patterns. The *d* value for (002) plane of g-C<sub>3</sub>N<sub>4</sub> and hybrid samples were summarized in Table 2. The difference of *d* value between original g-C<sub>3</sub>N<sub>4</sub> and g-C<sub>3</sub>N<sub>4</sub> in hybrid samples was hardly recognized. Therefore, we concluded that the structural change of g-C<sub>3</sub>N<sub>4</sub> in the hybrid photocatalysts was not occurred after the three kinds of mixture treatments.

Table 2 *d* value of hybrid photocatalyst and their original compound

Name	Treatment	<i>d</i> value / nm
g-C <sub>3</sub> N <sub>4</sub>	No treatment	0.3243
a-CW	Agate mortar	0.3232
s-CW	Sonication	0.3238
p-CW	Planetary mill	0.3239

FT-IR spectra of g-C<sub>3</sub>N<sub>4</sub> and hybrid photocatalysts were shown in Fig. S2. We observed the typical peaks assigned to g-C<sub>3</sub>N<sub>4</sub> for all samples. The detailed assignments of the peaks were as follows. The characteristic-breathing mode of the triazine units was observed at 820 cm<sup>-1</sup>[46]. The peaks attributed to the stretching vibration modes of heptazine-derived repeating units were observed at 1600, 1500, and 1440 cm<sup>-1</sup>. The peaks at 1350 and 1280 cm<sup>-1</sup> were assigned to stretching vibration of connected trigonal units or secondary amine. These results indicated that the characteristic structure of g-C<sub>3</sub>N<sub>4</sub> was stable even after the mixture process.

Figure 3 shows SEM micrographs of the morphologies of hybrid photocatalysts as well as original g-C<sub>3</sub>N<sub>4</sub> and WO<sub>3</sub>. WO<sub>3</sub> showed aggregated particles with particle size of several hundreds of nanometers (Fig. 3a), while g-C<sub>3</sub>N<sub>4</sub> was plate-like particles with particle size of more than several μm (Fig. 3b). By treatment with a planetary mill, g-C<sub>3</sub>N<sub>4</sub> plate particles were pulverized into particles of smaller sizes (not shown here). In addition, S<sub>BET</sub> of g-C<sub>3</sub>N<sub>4</sub> was increased after planetary mill treatment (Table 1). This property change agrees with the results of a previous study showing that S<sub>BET</sub> of g-C<sub>3</sub>N<sub>4</sub> was increased by ball mill treatment due to decrease in particle size [47]. On the other hand, the morphology and S<sub>BET</sub> of WO<sub>3</sub> did not change after planetary mill treatment. In the sample prepared by an agate mortar and sonication method (a-CW and s-CW), two obviously different morphologies of particles were easily recognized, and they are assigned to g-C<sub>3</sub>N<sub>4</sub>, respectively, because the morphology of WO<sub>3</sub> is quite different from that of g-C<sub>3</sub>N<sub>4</sub>. Agglomerated



WO<sub>3</sub> particles were loaded on plate-like g-C<sub>3</sub>N<sub>4</sub> (Fig. 3c, d). In contrast, the mixture condition between WO<sub>3</sub> and g-C<sub>3</sub>N<sub>4</sub> was greatly improved by planetary mill treatment (p-CW) and it seemed that g-C<sub>3</sub>N<sub>4</sub> particles were covered by highly dispersed WO<sub>3</sub> (Fig. 3e). This indicates that pulverized g-C<sub>3</sub>N<sub>4</sub> and WO<sub>3</sub> were highly mixed during planetary mill treatment. These results agree with previously reported results about a similar hybrid photocatalytic system for degradation of pollutants [48].

### 3.2. Photocatalytic activity for CO<sub>2</sub> reduction

The main product of CO<sub>2</sub> reduction was CH<sub>3</sub>OH in liquid phase, while trace amounts of HCOOH in liquid phase, H<sub>2</sub>, CO and CH<sub>4</sub> in gas phase were also detected. Figure 4 shows CH<sub>3</sub>OH production over the photoirradiated prepared hybrid photocatalysts with different contents of g-C<sub>3</sub>N<sub>4</sub> and WO<sub>3</sub> as well as pure g-C<sub>3</sub>N<sub>4</sub> and pure WO<sub>3</sub>.

No kinds of products were detected over the photocatalysts including the hybrid photocatalyst, g-C<sub>3</sub>N<sub>4</sub>, and WO<sub>3</sub> under nitrogen atmosphere instead of CO<sub>2</sub> under photoirradiation. In addition, these photocatalysts did not show any activity for CO<sub>2</sub> reduction in a dark condition. Photoreduction of CO<sub>2</sub> did not proceed in the absence of photocatalysts even under photoirradiation.

No products such as CH<sub>3</sub>OH by photoreduction of CO<sub>2</sub> were observed in the case of pure WO<sub>3</sub> because the conduction band potential of WO<sub>3</sub> is too low for CO<sub>2</sub> reduction to proceed in aqueous media. On the other hand, g-C<sub>3</sub>N<sub>4</sub> showed relatively high activity for CO<sub>2</sub> reduction. Photocatalytic activity of the prepared hybrid photocatalyst at the optimized mixture ratio of g-C<sub>3</sub>N<sub>4</sub> and WO<sub>3</sub> for CH<sub>3</sub>OH production as a result of CO<sub>2</sub> reduction was 2.4-times higher than that of pure g-C<sub>3</sub>N<sub>4</sub> as shown in Figure 5. If the two kinds of photocatalyst were just physically mixed, photocatalytic activity of the hybrid photocatalyst should be lower than that of g-C<sub>3</sub>N<sub>4</sub>. Therefore, we concluded that the dramatic improvement in photocatalytic activity of the hybrid photocatalyst is due to efficient charge separation between two kinds of photocatalysts through a Z-scheme mechanism mimicking artificial photosynthesis. In order to elucidate electron behavior between the two kinds of photocatalyst, DB-PAS measurements were performed. We also analyzed the source of carbon of CH<sub>3</sub>OH in order to obtain direct evidence for CO<sub>2</sub> reduction by <sup>1</sup>H-NMR for isotope analyses of <sup>13</sup>CO<sub>2</sub>. These issues will be discussed in detail in a later section.

### 3.3. Effect of co-catalyst loading on photocatalytic activity

For further improvement of photocatalytic efficiency for CO<sub>2</sub> reduction, Au or Ag particles as co-catalysts were loaded only on g-C<sub>3</sub>N<sub>4</sub> of the prepared hybrid photocatalysts by photodeposition because g-C<sub>3</sub>N<sub>4</sub> works as a reduction photocatalyst for CO<sub>2</sub> reduction, whereas water oxidation as a

counter reaction of CO<sub>2</sub> reduction might proceed on WO<sub>3</sub>.

After photodeposition, the color of the samples changed depending on the kind of loading metal and loading amount. The both of Au-loaded and Ag-loaded samples immediately after photodeposition were both reddish color. The colors of the samples are assigned to localized surface plasmon resonance (LSPR) absorption of Au and Ag [49-51], and these properties indicated that most of the Au and Ag particles were loaded as a metal state. Figure 6 shows DR spectra of the prepared hybrid photocatalysts loaded with Au and Ag nanoparticles. An absorption peak around 550 nm, is assigned to LSPR of Au on g-C<sub>3</sub>N<sub>4</sub> of the hybrid photocatalyst, was observed in the Au-loaded hybrid sample as shown in Fig.6 (a) [49-51]. However, steep LSPR absorption of Ag on g-C<sub>3</sub>N<sub>4</sub> of the hybrid photocatalyst was not observed (Fig. 6 (b)). An LSPR absorption peak of Ag nanoparticles is usually observed at around 450 nm. The absorption peak assigned to LSPR absorption of Ag and the optical absorption of the hybrid sample might be overlapped, resulting in disappearance of the LSPR absorption peak of Ag nanoparticles. XPS measurements were also carried out to analyze the valence states of Au and Ag loaded on the hybrid samples. XPS spectra showed that loaded Ag particles were present as a mixture of Ag and AgO. In contrast, the XPS spectrum of Au particles loaded on the hybrid photocatalysts was assigned to metal without other valence states.

Figure 7 shows the photocatalytic activities for CH<sub>3</sub>OH generation over the prepared hybrid photocatalysts loaded with Au and Ag. The amount of CH<sub>3</sub>OH generated by CO<sub>2</sub> reduction showed a volcano-like relationship with amount of co-catalyst loading. The optimum amount of Au or Ag loading for CH<sub>3</sub>OH generation was 0.5 wt%, respectively. Increase in generation of CH<sub>3</sub>OH by CO<sub>2</sub> reduction was presumably due to prevention of recombination and/or improvement of selectivity for CO<sub>2</sub> reduction by electron capturing on metal particles because reduction of protons to hydrogen usually competes with the CO<sub>2</sub> reduction. Decrease in CH<sub>3</sub>OH generation with an excess amount of the co-catalyst may be due to lowering of dispersibility and increase in particle size of the co-catalyst.

In order to elucidate the influence of Au or Ag particle size on CH<sub>3</sub>OH generation, photoabsorption peaks attributed to LSPR of Au particles were evaluated in UV-VIS spectra (Fig. 6). Figure 6 shows absorption wavelength of the peak (*I<sub>p</sub>*) attributed to LSPR of Au loaded on g-C<sub>3</sub>N<sub>4</sub> as a function of amount of co-catalyst loading. The wavelength of the peak might be affected by particle size and aggregation state of metal particles [34-36]. The peaks of Au-loaded samples showed dependence on loading amount up to 1.0 wt%. This indicates that decrease in CH<sub>3</sub>OH generation by the 1.0 wt% Au-loaded sample might be due to change in Au particle size. Therefore, CH<sub>3</sub>OH generation of the Au-loaded sample was influenced by particle size and/or

aggregation state.

Figure S4 shows HCOOH generation of the prepared hybrid photocatalysts with Au loading. HCOOH generation decreased with an increase in Au loading amount. This indicates that Au loading may enhance selectivity for CH<sub>3</sub>OH generation, though the decreased amount of HCOOH was much smaller than the increased amount of CH<sub>3</sub>OH by Au loading. On the other hand, Ag-loaded samples showed a volcano-like relationship similar to that for CH<sub>3</sub>OH generation. This indicates that Au loading induces no selectivity for CH<sub>3</sub>OH generation but works effectively for capturing electrons. In the case of Ag loaded hybrid photocatalyst, trace amounts of HCOOH in liquid phase, H<sub>2</sub>, CO and CH<sub>4</sub> in gas phase were also observed, whose amounts are lower than detection limit of gas and ion chromatography.

### 3.5. DB-PA spectroscopic detection of electron behavior under visible-light irradiation

In order to clarify that the synergistic effect is due to charge transfer between two kinds of semiconductors, DB-PA spectroscopy measurements were carried out. The behavior of electrons in a metal oxide semiconductor was observed by DB-PAS [27]. At first, time-course curves of PA intensity for p-CW as well as WO<sub>3</sub> and g-C<sub>3</sub>N<sub>4</sub> at the ratios of 100 : 0 – 0 : 100 in the presence of EtOH under N<sub>2</sub> + O<sub>2</sub> atmosphere ( $I_{N_2+O_2}$ ) were measured as shown Fig. 8. Increase in PA intensity of pure WO<sub>3</sub> was observed under visible-light irradiation because W<sup>6+</sup> was reduced to W<sup>5+</sup> by excitation of electrons in the conduction band of WO<sub>3</sub> (Fig. 8). Thus, change in PA intensity under visible light is attributed to the amount of trapped electrons (W<sup>5+</sup>) in WO<sub>3</sub>. Figure 9 shows the relation between amount ratio (wt/wt) of g-C<sub>3</sub>N<sub>4</sub> and WO<sub>3</sub> and the saturation limit of PA intensity under N<sub>2</sub> + O<sub>2</sub> + EtOH ( $I_{N_2+O_2}$ ). The  $I_{N_2+O_2}$  of the hybrid photocatalysts composed of g-C<sub>3</sub>N<sub>4</sub> and WO<sub>3</sub> was smaller than that expected intensity from the calculated value of content ratio of g-C<sub>3</sub>N<sub>4</sub> and WO<sub>3</sub> under visible-light irradiation because the trapped electrons (W<sup>5+</sup>) was partially reacted with holes in valence band of g-C<sub>3</sub>N<sub>4</sub> resulting in annihilation.

In the case of p-CW, plausible charge transfer under visible-light irradiation is only electron injection from the conduction band of g-C<sub>3</sub>N<sub>4</sub> to the conduction band of WO<sub>3</sub>. Under that condition, the photocatalytic activity of p-CW should be lower than that of pure p-g-C<sub>3</sub>N<sub>4</sub>. However, experimentally determined photocatalytic activity over photoirradiated p-CW for reduction of CO<sub>2</sub> was much higher than that of p-g-C<sub>3</sub>N<sub>4</sub> and p-WO<sub>3</sub>. This result suggests that electron injection from g-C<sub>3</sub>N<sub>4</sub> to WO<sub>3</sub> does not proceed over p-CW (Fig. 10a). In contrast, a Z-scheme reaction also possibly proceeds over p-CW (Fig. 10b) in addition to the above charge separation model. The smaller PA intensity of p-CW than that of g-C<sub>3</sub>N<sub>4</sub> and WO<sub>3</sub> and the higher photocatalytic activity of p-CW than that of g-C<sub>3</sub>N<sub>4</sub> and WO<sub>3</sub> indicate that the Z-scheme model was

the main charge transfer path over p-CW rather than the charge separation model. As a result, p-CW can possess both high oxidation ability of  $\text{WO}_3$  and high reduction ability of g- $\text{C}_3\text{N}_4$ . Smaller PA intensities of p-CW at any content ratio of g- $\text{C}_3\text{N}_4$  and  $\text{WO}_3$  than those of g- $\text{C}_3\text{N}_4$  and  $\text{WO}_3$  were observed. This indicates that photocatalytic activity strongly depended on Z-scheme charge transfer and that a large number of contact points are important for efficient charge transfer.

Fig. S5 shows the amount of increase in PA intensity of the hybrid photocatalyst prepared in an agate mortar. Unlike the case of PA intensity of the hybrid photocatalyst prepared in a planetary mill, the calculated value of PA intensity and the experimental value are almost identical in the case of hybrid photocatalysts prepared by an agate mortar (Fig. S6). PA intensity increase with increase in the amount of  $\text{WO}_3$ , which is assigned to trapped electrons in the conduction band of  $\text{WO}_3$ , indicated that the Z scheme process did not proceed in the case of hybrid photocatalysts prepared by the agate mortar. In other words, electron transfer between  $\text{WO}_3$  and g- $\text{C}_3\text{N}_4$  did not occur because the two kinds of photocatalyst were just physically mixed.

### 3.6. Labeling experiments using $^{13}\text{CO}_2$ reduction of $\text{CO}_2$

In the  $^1\text{H}$  NMR of Ag or Au-loaded hybrid photocatalysts (with 0.5 wt% loading), a doublet ( $J_{\text{CH}} = 142$  Hz) attributable to the proton coupled to the  $^{13}\text{C}$  of  $^{13}\text{CH}_3\text{O}^-$  was observed at 3.34 ppm, but no singlet due to the proton of  $^{12}\text{CH}_3\text{O}^-$  was detected (Fig 11). These results clearly show that the carbon source of  $\text{CH}_3\text{OH}$  is incorporated from  $\text{CO}_2$ .

## 4. Conclusions

A highly active hybrid photocatalyst under visible-light irradiation for  $\text{CO}_2$  reduction was prepared by hybridization with g- $\text{C}_3\text{N}_4$  and  $\text{WO}_3$  using a planetary mill. Planetary mill treatment increased  $S_{\text{BET}}$  and the number of contact points for charge transfer between the two semiconductors. DB-PAS measurements revealed that Z-scheme charge transfer occurred over that p-CW under visible-light irradiation and p-CW can utilize both the high oxidation ability of  $\text{WO}_3$  and high reduction ability of g- $\text{C}_3\text{N}_4$ .

## Acknowledgment.

This work was supported by JST PRESTO program and JST ACT-C program.

Figure captions

Figure 1. Diffuse reflectance (DR) spectrum of milled g-C<sub>3</sub>N<sub>4</sub>, milled WO<sub>3</sub> and the hybrid photocatalyst composed of g-C<sub>3</sub>N<sub>4</sub> and WO<sub>3</sub> at the ratio of 1 : 1 (p-CW)

Figure 2. XRD pattern of g-C<sub>3</sub>N<sub>4</sub> and hybrid photocatalysts

Figure 3. SEM images of (a) WO<sub>3</sub>, (b) g-C<sub>3</sub>N<sub>4</sub>, (c) a-CW, (d) s-CW and (e) p-CW.

Figure 4. CH<sub>3</sub>OH generation of the hybrid photocatalyst composed of g-C<sub>3</sub>N<sub>4</sub> and WO<sub>3</sub> with a ratio of 1:1, g-C<sub>3</sub>N<sub>4</sub> and commercial WO<sub>3</sub>.

Figure 5. CH<sub>3</sub>OH generation of the hybrid photocatalyst as a function of the content ratio of g-C<sub>3</sub>N<sub>4</sub> and WO<sub>3</sub>.

Figure 6. DR spectra of the hybrid photocatalysts loaded with Au (a) or Ag (b) nanoparticles at different contents.

Figure 7. CH<sub>3</sub>OH generation of the Au or Ag loaded hybrid photocatalyst composed of g-C<sub>3</sub>N<sub>4</sub> and WO<sub>3</sub> with a ratio of 1:2, g-C<sub>3</sub>N<sub>4</sub> and commercial WO<sub>3</sub>.

Figure 8. Time-course curves of PA signals of the hybrid photocatalysts composed of WO<sub>3</sub> and g-C<sub>3</sub>N<sub>4</sub> with different contents, which was prepared by a planetary mill, g-C<sub>3</sub>N<sub>4</sub> and commercial WO<sub>3</sub> under visible light irradiation in the presence of EtOH under N<sub>2</sub> + O<sub>2</sub> atmosphere.

Figure 9. The relation between amount ratio (wt/wt) of g-C<sub>3</sub>N<sub>4</sub> and WO<sub>3</sub> in the hybrid photocatalysts prepared by a planetary mill and saturation limit of PA intensity under N<sub>2</sub> + O<sub>2</sub> + EtOH (*I*<sub>N<sub>2</sub>+O<sub>2</sub></sub>).

Dashed line: calculation value, black circle: experimental value

Figure 10. Suggested photocatalytic reaction schemes of the hybrid photocatalysts.

(a) Charge separation type and (b) Z scheme type

Figure 11. <sup>1</sup>H-NMR spectra of the reaction solutions (<sup>13</sup>CO<sub>2</sub> saturated D<sub>2</sub>O) were observed after 24-h irradiation by LED at 435 nm. Au (a) or Ag (b) loaded hybrid photocatalysts was used as photocatalyst. <sup>1</sup>H-NMR spectra of <sup>12</sup>CH<sub>3</sub>OH (c) and <sup>13</sup>CH<sub>3</sub>OH (d) in D<sub>2</sub>O was also analyzed as reference.

Figure S1. Process of experiments using <sup>13</sup>CO<sub>2</sub> reduction of CO<sub>2</sub>

Figure S2. FT-IR spectra of g-C<sub>3</sub>N<sub>4</sub> and hybrid photocatalysts

Figure S3. SEM image of the Au or Ag loaded g-C<sub>3</sub>N<sub>4</sub> (0.5 and 1.0 wt%) and the Au or Ag loaded hybrid photocatalyst composed of g-C<sub>3</sub>N<sub>4</sub> and WO<sub>3</sub> (0.5 wt%)

Figure S4. HCOOH generation of the Au loaded hybrid photocatalyst composed of g-C<sub>3</sub>N<sub>4</sub> and WO<sub>3</sub> with a ratio of 1:2.

Figure S5. Time-course curves of PA signals of the hybrid photocatalysts composed of WO<sub>3</sub> and g-C<sub>3</sub>N<sub>4</sub> with different contents, which was prepared by an agate mortar, g-C<sub>3</sub>N<sub>4</sub> and commercial

WO<sub>3</sub> under visible light irradiation in the presence of EtOH under N<sub>2</sub> + O<sub>2</sub> atmosphere.

Figure S6. The relation between amount ratio (wt/wt) of g-C<sub>3</sub>N<sub>4</sub> and WO<sub>3</sub> in the hybrid photocatalysts prepared by an agate mortar and saturation limit of PA intensity under N<sub>2</sub> + O<sub>2</sub> + EtOH ( $I_{N_2+O_2}$ ).

Dashed line: calculation value, black circle: experimental value

## References

- [1] O. K. Varghese, M. Paulose, T. J. LaTempa, C. A. Grimes, *Nano Lett.* 9 (2009) 731–737.
- [2] J. Y. Liu, B. Garg, Y. C. Ling, *Green Chem.* 13 (2011) 2029–2031.
- [3] T. Inoue, A. Fujishima, S. Konishi, K. Honda, *Nature* 277 (1979) 637–638.
- [4] F. Solymosi, I. Tombácz, *Catal. Lett.* 27 (1994) 61–65.
- [5] M. Anpo, H. Yamashita, Y. Ichihashi, Y. Fujii, M. Honda, *J. Phys. Chem. B* 101 (1997) 2632–2636.
- [6] I. H. Tseng, J. C. S. Wu, H. Y. Chou, *J. Catal.* 221 (2004) 432–440.
- [7] Q. H. Zhang, W. D. Han, Y. J. Hong, J. G. Yu, *Catal. Today* 148 (2009) 335–340.
- [8] K. Koci, K. Mateju, L. Obalova, S. Krejčíková, Z. Lacny, D. Placha, L. Capek, A. Hospodkova, O. Solcova, *Appl. Catal. B: Environ.* 96 (2010) 239–244.
- [9] T. Yui, A. Kan, C. Saitoh, K. Koike, T. Ibusuki, O. Ishitani, *ACS Appl. Mater. Interfaces* 3 (2011) 2594–2600.
- [10] K. Sayama, H. Arakawa, *Phys. Chem.* 97 (1993) 531–533.
- [11] Y. Matsumoto, M. Obata, J. Hombo, *J. Phys. Chem.* 98 (1994) 2950–2951.
- [12] P.W. Pan, Y.W. Chen, *Catal. Commun.* 8 (2007) 1546–1549.
- [13] Q. Liu, Y. Zhou, J. Kou, X. Chen, Z. Tian, J. Gao, S. Yan, Z. Zou, *J. Am. Chem. Soc.* 132 (2010) 14385–14387.
- [14] S. C. Yan, S. X. Ouyang, J. Gao, M. Yang, J. Y. Feng, X. X. Fan, L. J. Wan, Z. S. Li, J. H. Ye, Y. Zhou, Z. G. Zou, *Angew. Chem. Int. Ed.* 49 (2010) 6400–6404.
- [15] Y. Zhou, Z. Tian, Z. Zhao, Q. Liu, J. Kou, X. Chen, J. Gao, S. Yan, Z. Zou, *ACS Appl. Mater. Interfaces* 3 (2011) 3594–3601.
- [16] K. Iizuka, T. Wato, Y. Miseki, K. Saito, A. Kudo, *J. Am. Chem. Soc.* 133 (2011) 20863–20868.
- [17] K. Maeda, X. Wang, Y. Nishihara, D. Lu, M. Antonietti, K. Domen, *J. Phys. Chem. C* 133(12) (2009) 4940–4947.
- [18] X. C. Wang, K. Maeda, A. Thomas, K. Takanabe, G. Xin, J. M. Carlsson, K. Domen, M. Antonietti, *Nat. Mater.* 8 (2009) 76–80.
- [19] J. Lin, Z. Pan, X. Wang, *ACS Sustainable Chem. Eng.* 10 (2013) 1021.
- [20] K. Maeda, K. Sekizawa, O. Ishitani, *Chem. Commun.* 49 (2013) 10127–10129.
- [21] Z. Huang, F. Li, B. Chen, T. Lu, Y. Yuan, G. Yuan, *Appl. Catal., B* 136–137 (2013) 269–277.
- [22] Y. Zheng, J. Liu, J. Liang, M. Jaroniec, S. Z. Qiao, *Energy Environ. Sci.* 5 (2012) 6717–6731.
- [23] J. Zhang, M. Grzelczak, Y. Hou, K. Maeda, K. Domen, X. Fu, M. Antonietti, X. Wang, *Chem. Sci.* 3 (2012)

443-446.

- [24] Y. Wang, X. Wang, M. Antonietti, *Angew. Chem. Int. Ed.* 51 (2012) 68-89.
- [25] M. B. Ansari, B. H. Min, Y. H. Mo, S. E. Park, *Green Chem.* 13 (2011) 1416-1421.
- [26] S. S. Park, S. W. Chu, C. Xue, D. Zhao, C. S. Ha, *J. Mater. Chem.* 21 (2011) 10801-10807.
- [27] J. Zhang, X. Chen, K. Takanahe, K. Maeda, K. Domen, J. D. Epping, X. Fu, M. Antonietti, X. Wang, *Angew. Chem. Int. Ed.* 49 (2010) 441-444.
- [28] S. C. Yan, Z. S. Li, Z. G. Zou, *Langmuir* 25 (17) (2009) 10397-10401.
- [29] G. H. Dong, L. Z. Zhang, *J. Mater. Chem.* 22 (2012) 1160-1166.
- [30] J. Mao, T. Peng, X. Zhang, K. Li, L. Ye, L. Zan, *Catal. Sci. Technol.* 3 (2013) 1253-1260.
- [31] N. Serpone, P. Maruthamuthu, P. Pichat, E. Pelizzetti, H. Hidaka, *J. Photochem. Photobiol., A* 85 (1995) 247-255.
- [32] T. Tatsuma, S. Saitoh, P. Ngaotrakanwivat, Y. Ohko, A. Fujishima, *Langmuir* 18 (2002) 7777-7779.
- [33] Y. Takahashi, T. Tatsuma, *Langmuir* 21 (2005) 12357-12361.
- [34] Y. Bessekhoud, D. Robert, J. V. Weber, *Catal. Today* 101 (2005) 315-321.
- [35] T. Arai, M. Yanagida, Y. Konishi, Y. Iwasaki, H. Sugihara, K. Sayama, *J. Phys. Chem. C* 111 (2007) 7574-7577.
- [36] Z. Liu, Z. G. Zhao, M. Miyauchi, *J. Phys. Chem. C* 113 (2009) 17132-17137.
- [37] S. S. K. Ma, K. Maeda, R. Abe, K. Domen, *Energy Environ. Sci.* 5 (2012) 8390-8397.
- [38] M. Sadakane, N. Tamura, N. Kanome, S. Sumiya, R. Abe, T. Sano, *Chem. Lett.* 40 (2011) 443-445.
- [39] R. Abe, H. Takami, N. Murakami, B. Ohtani, *J. Am. Chem. Soc.* 130 (2008) 7780-7781.
- [40] D. Mitoraj, H. Kisch, *Chem. -Eur. J.* 16 (2010) 261-269.
- [41] S. C. Yan, S. B. Lv, Z. S. Li, Z. G. Zou, *Dalton Trans.* 39 (2010), 1488-1491.
- [42] H. Yan, Y. Huang, *Chem. Commun.* 47 (2011) 4168-4170.
- [43] A. Thomas, A. Fischer, F. Goettmann, M. Antonietti, J. O. Müller, R. Schlögl, J. M. Carlsson, *J. Mater. Chem.* 18 (2008) 4893-4908.
- [44] N. Murakami, O. O. P. Mahaney, R. Abe, T. Torimoto, B. Ohtani, *J. Phys. Chem. C* 111 (2007) 11927-11935.
- [45] F. Dong, L. W. Wu, Y. J. Sun, M. Fu, Z. B. Wu, S. C. Lee, *J. Mater. Chem.* 21 (2011) 15171-15174.
- [46] X. Li, M. Li, J. Yang, X. Li, T. Hu, J. Wang, Y. Sui, X. Wu, L. Kong, *J. Phys. Chem. Sol.*, 75 (2014) 441-446.
- [47] Y. Ming, F. Jianqing, H. Qiao, *J. Wuhan Univ. Technol., Mater. Sci. Ed.* 25 (2010) 914-918.
- [48] K. Kondo, N. Murakami, C. Ye, T. Tsubota, T. Ohno, *Appl. Catal., B* 142-143 (2013) 362-367.
- [49] Y. Tian, T. Tatsuma, *J. Am. Chem. Soc.* 127 (2005) 7632-7637.
- [50] K. Naoi, Y. Ohko, T. Tatsuma, *J. Am. Chem. Soc.* 126 (2004) 3664-3668.
- [51] A. Z. Jurek, E. Kowalska, J. W. Sobczak, W. Lisowski, B. Ohtani, A. Zaleska, *Appl. Catal., B* 101 (2011) 504-514.

Fig. 1

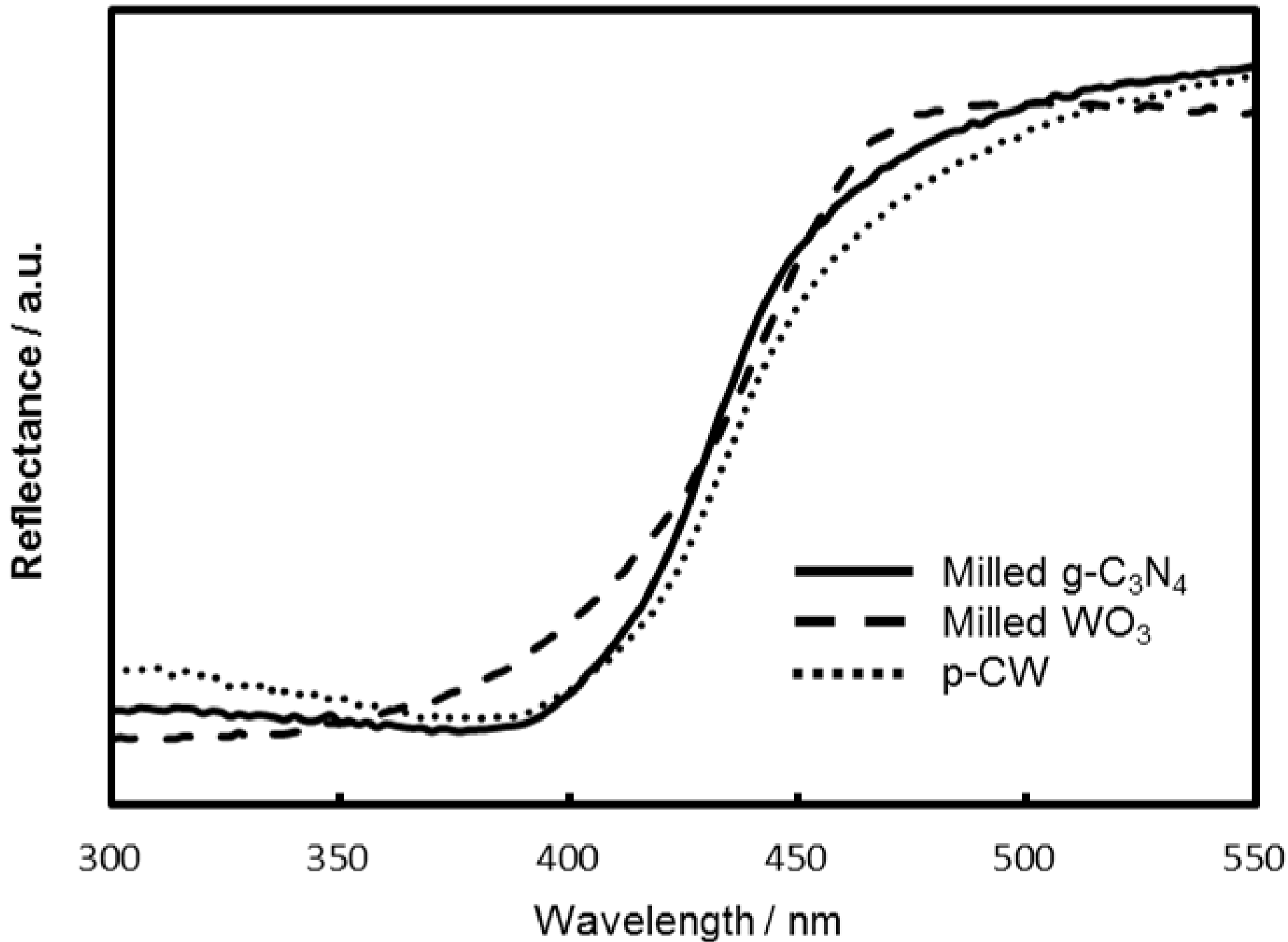




Fig. 2

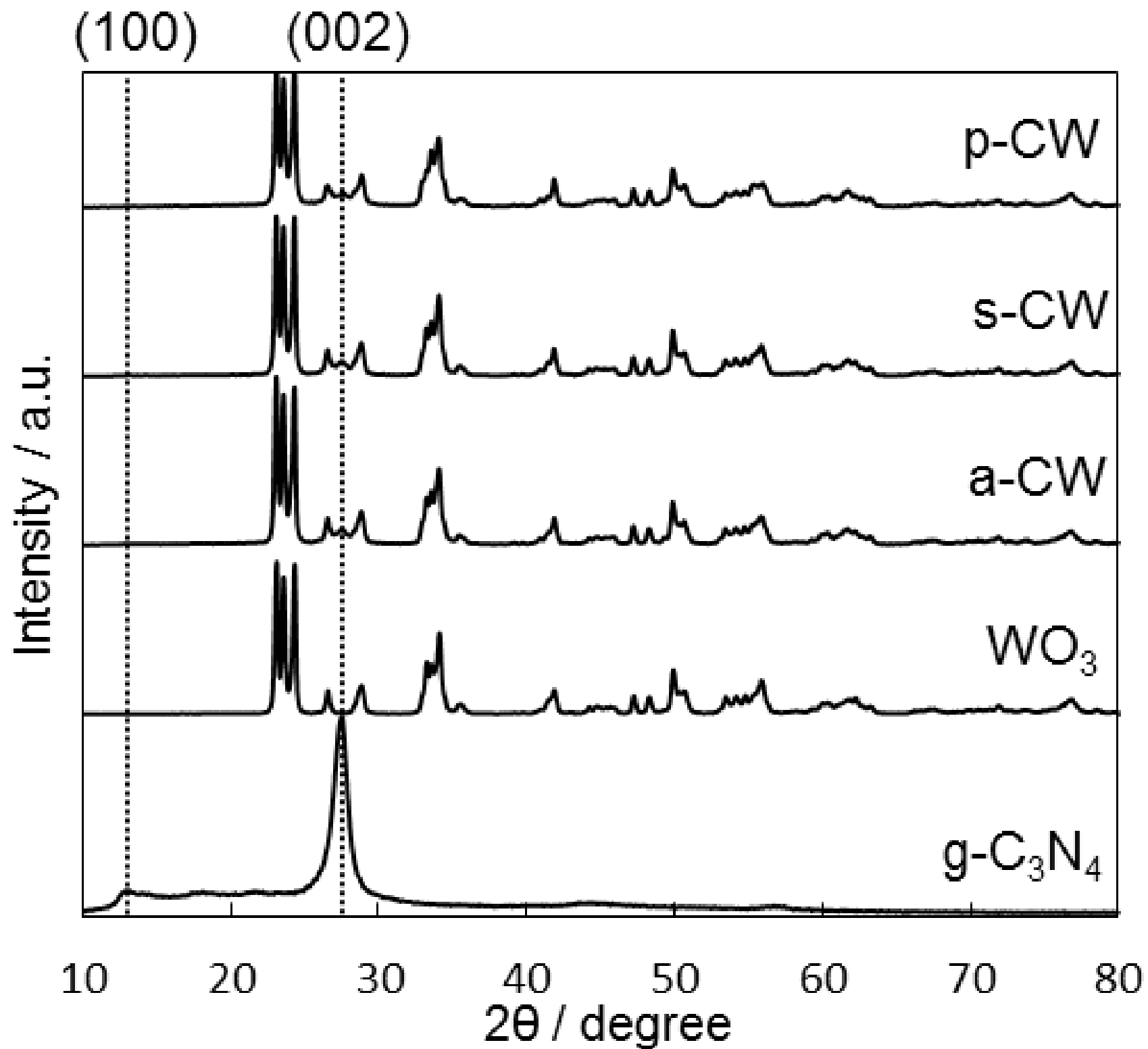
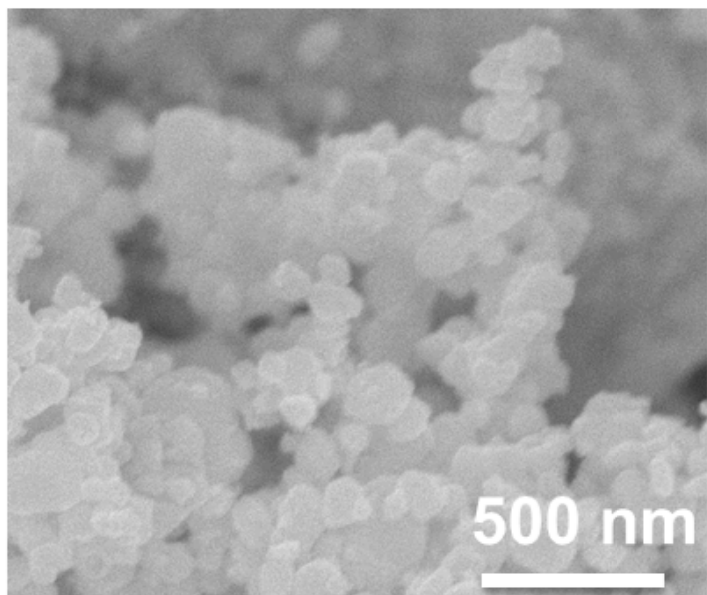
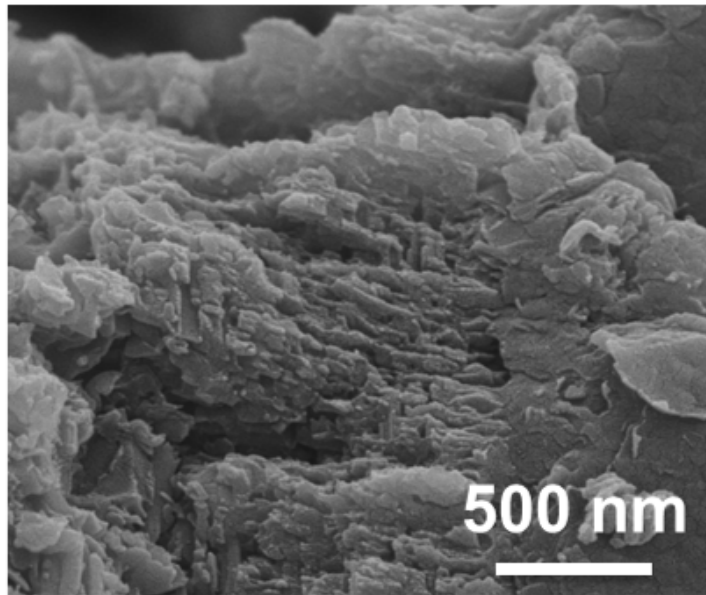


Fig. 3

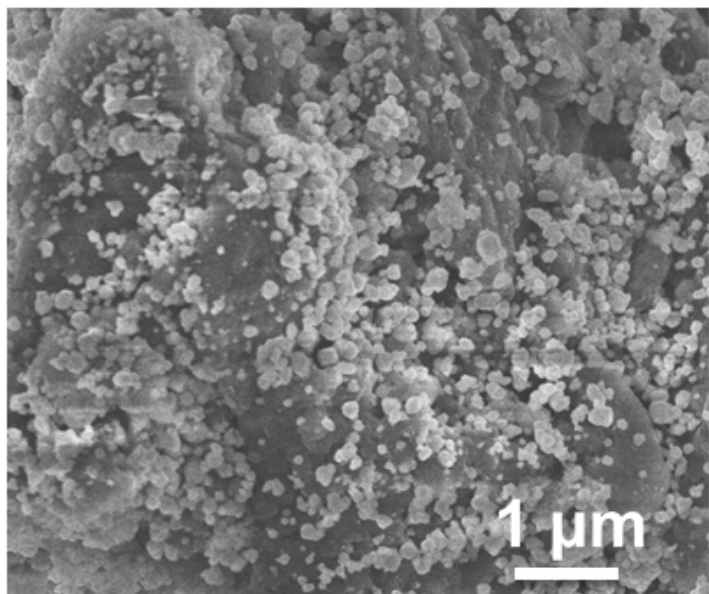
(a)



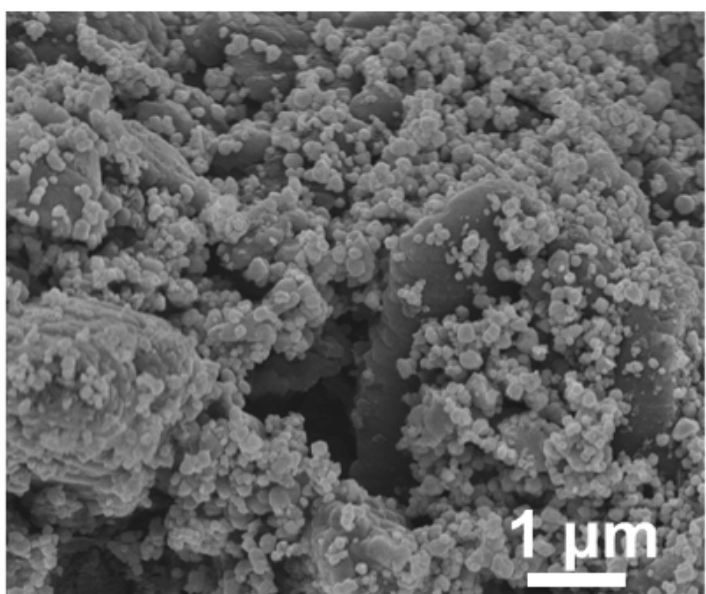
(b)



(c)



(d)



(e)

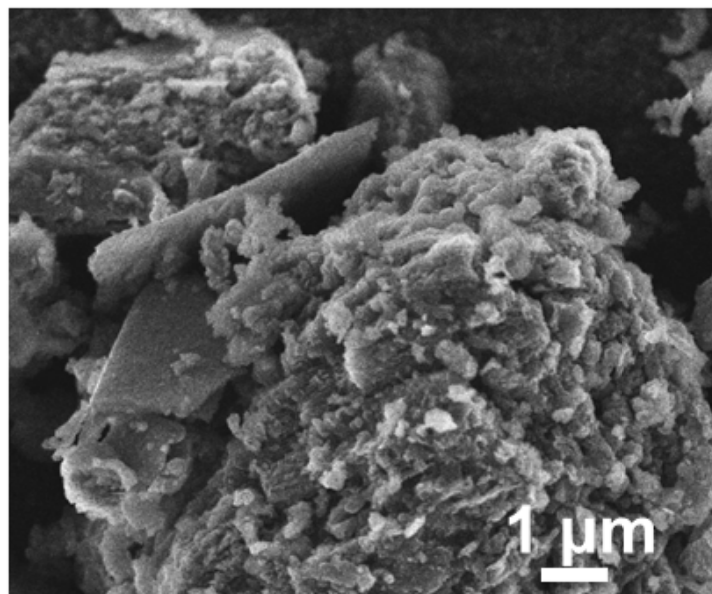


Fig. 4

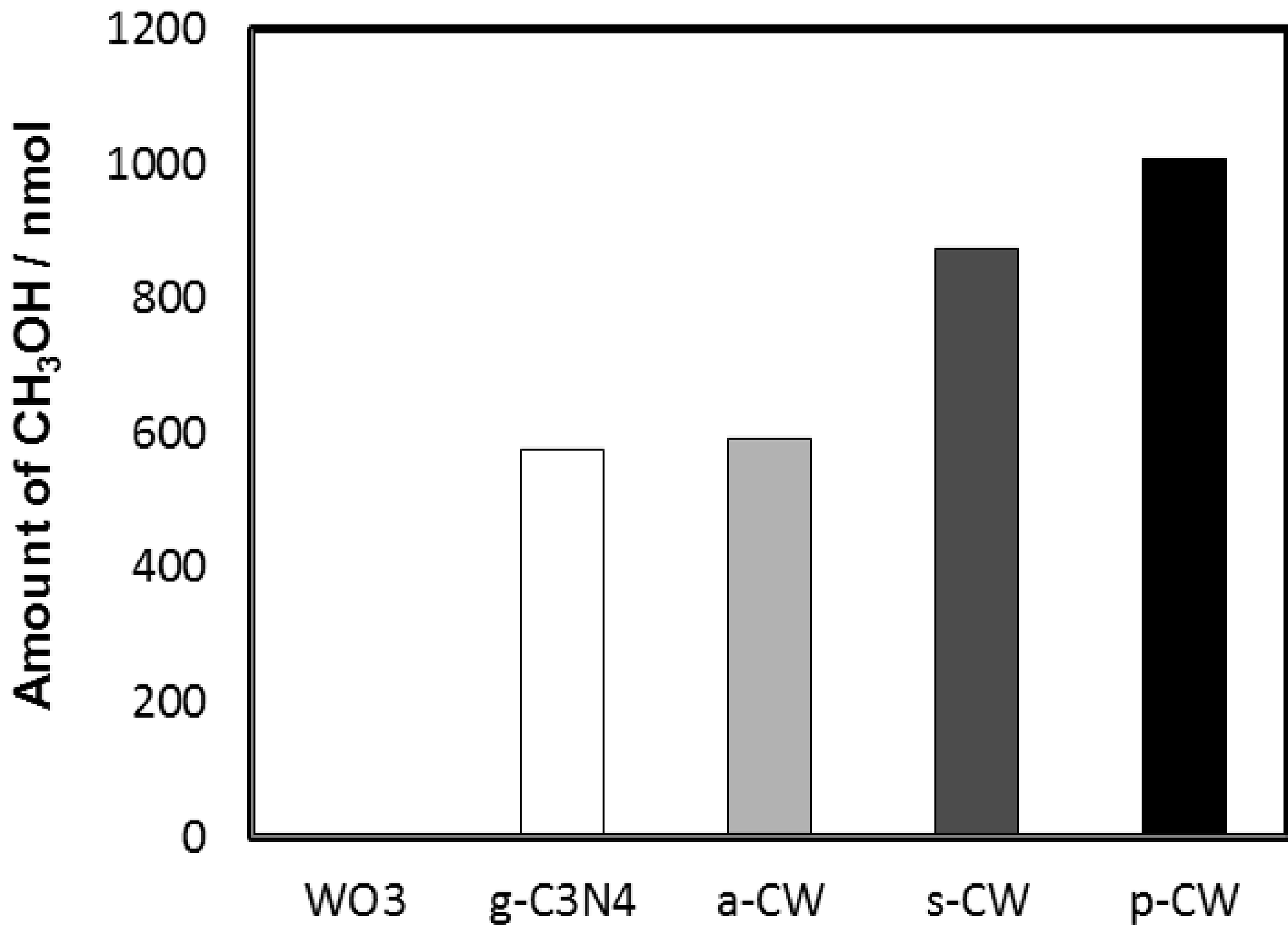


Fig. 5

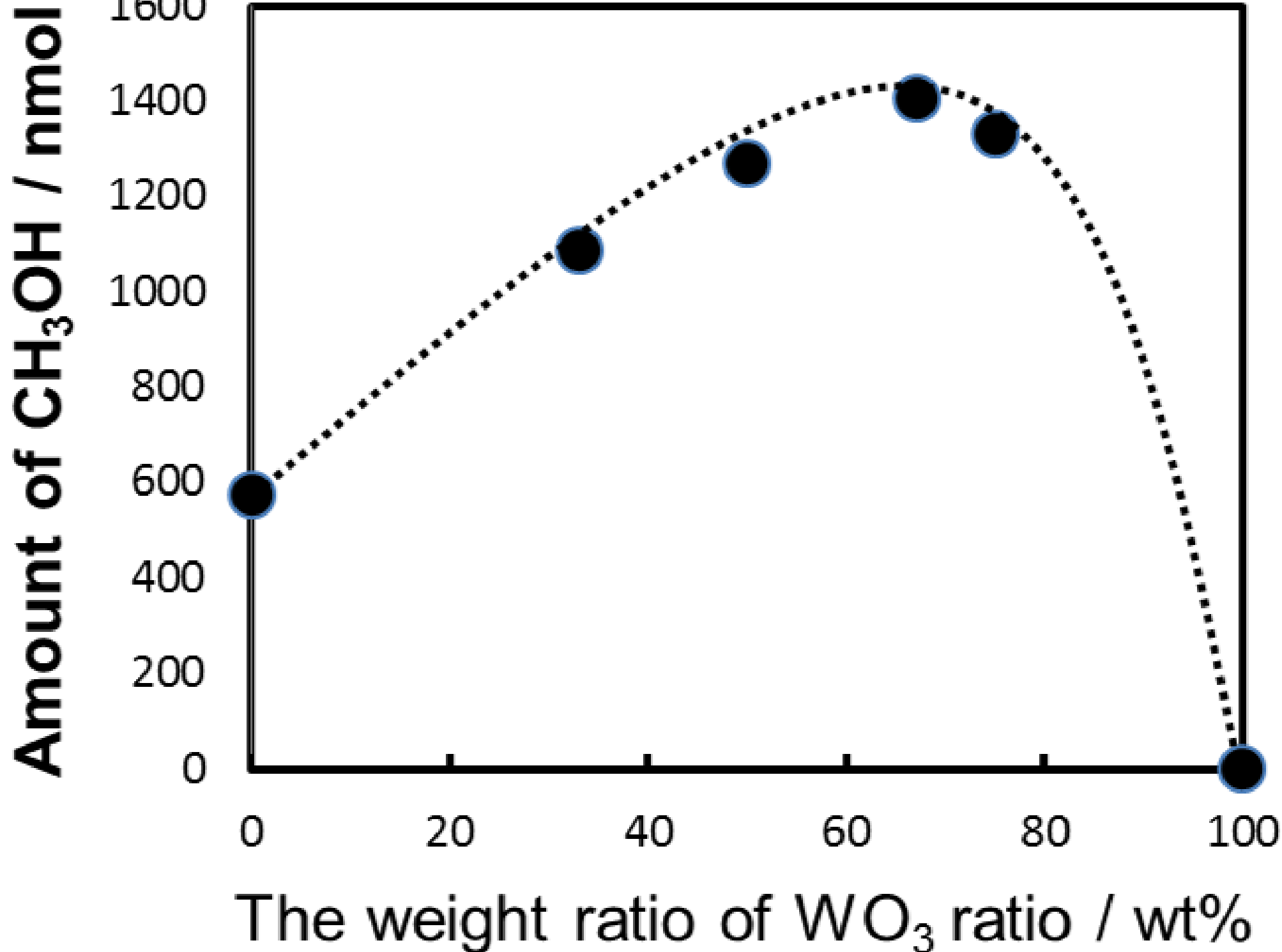


Fig. 6

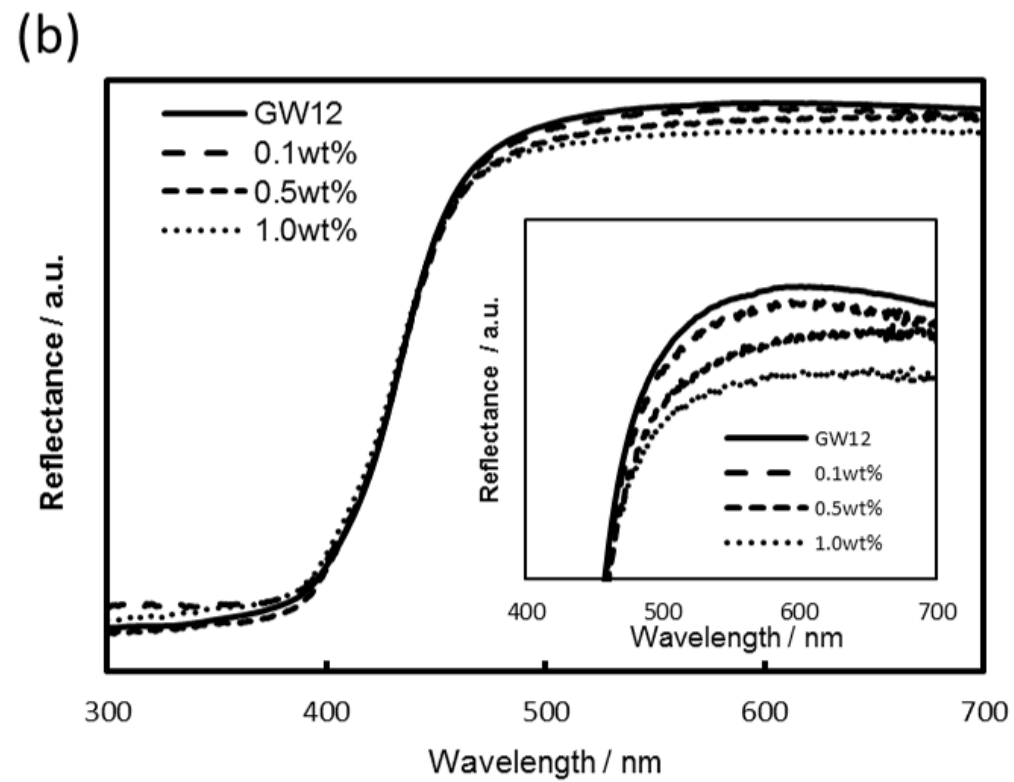
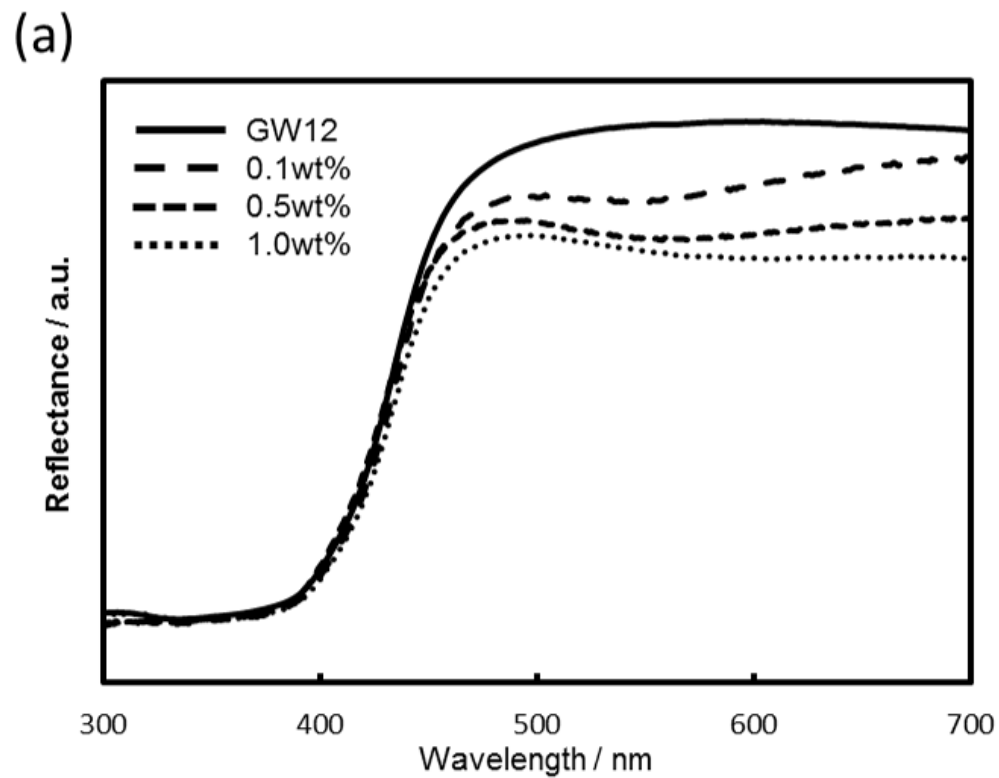


Fig. 7

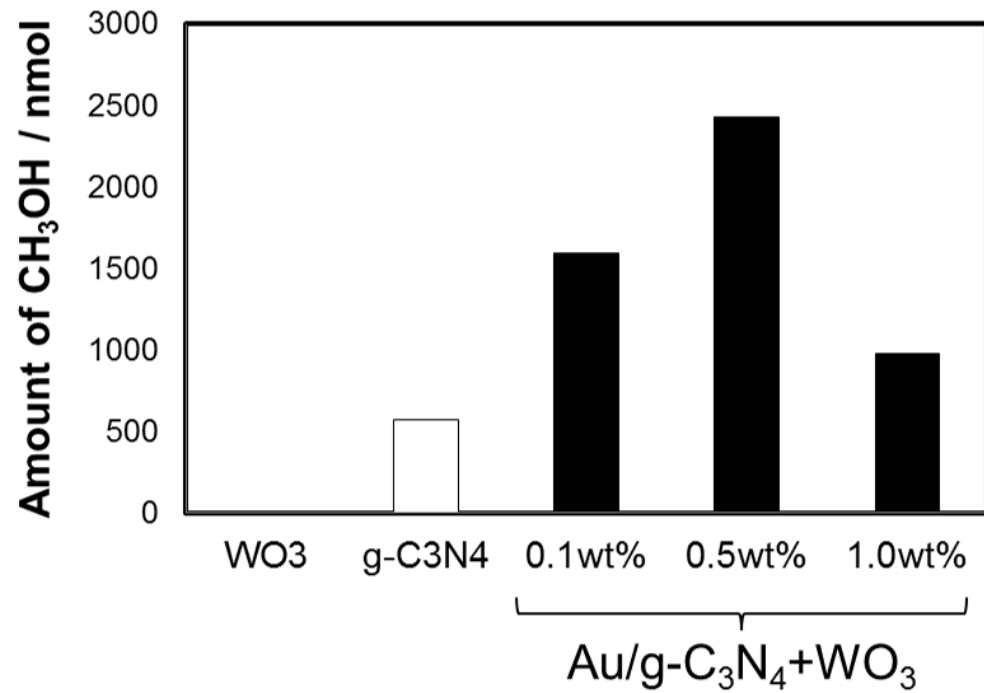
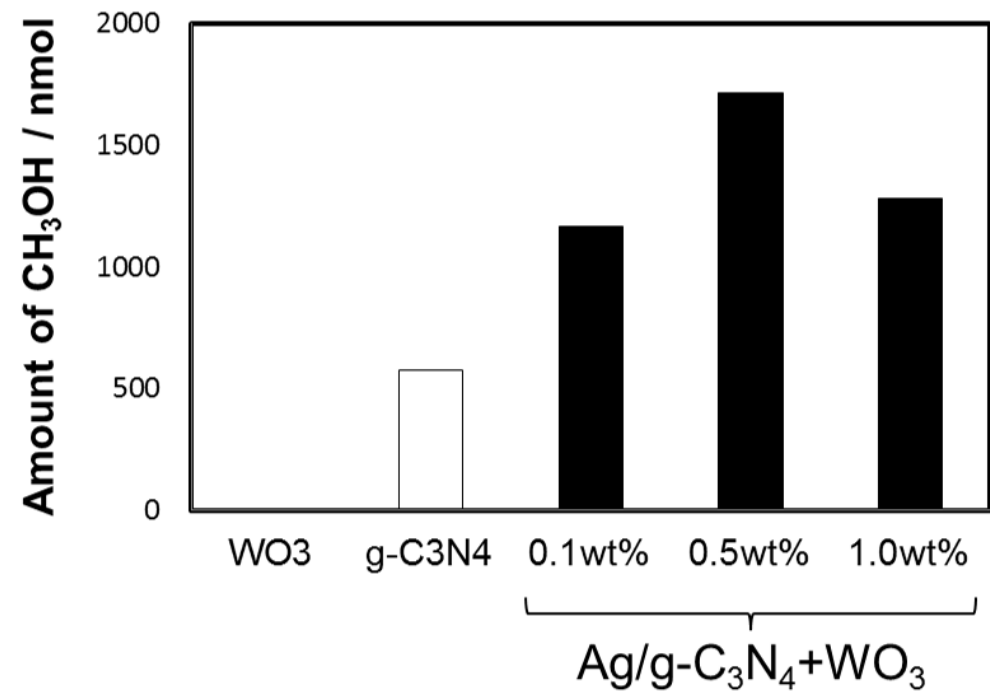


Fig. 8

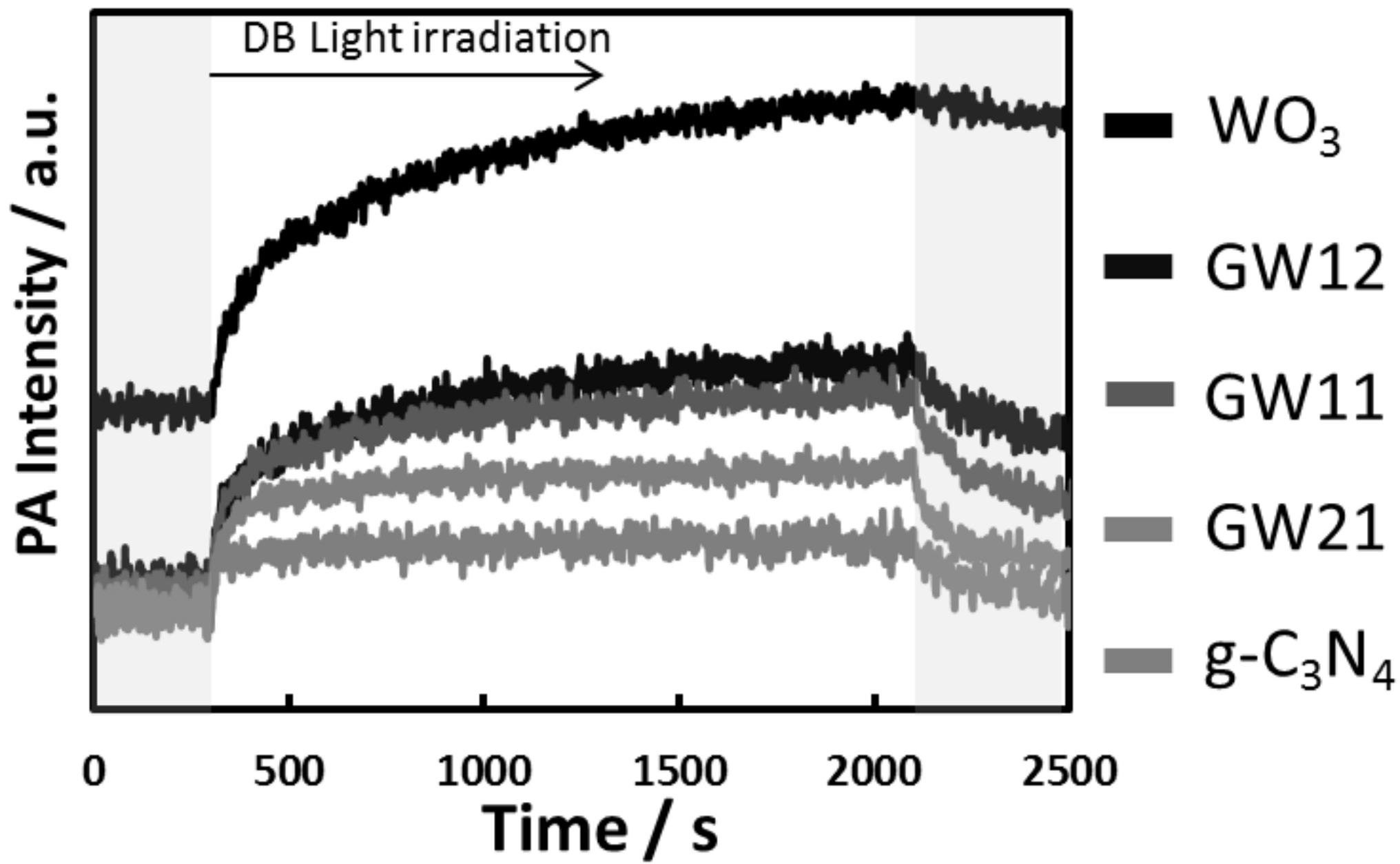


Fig. 9

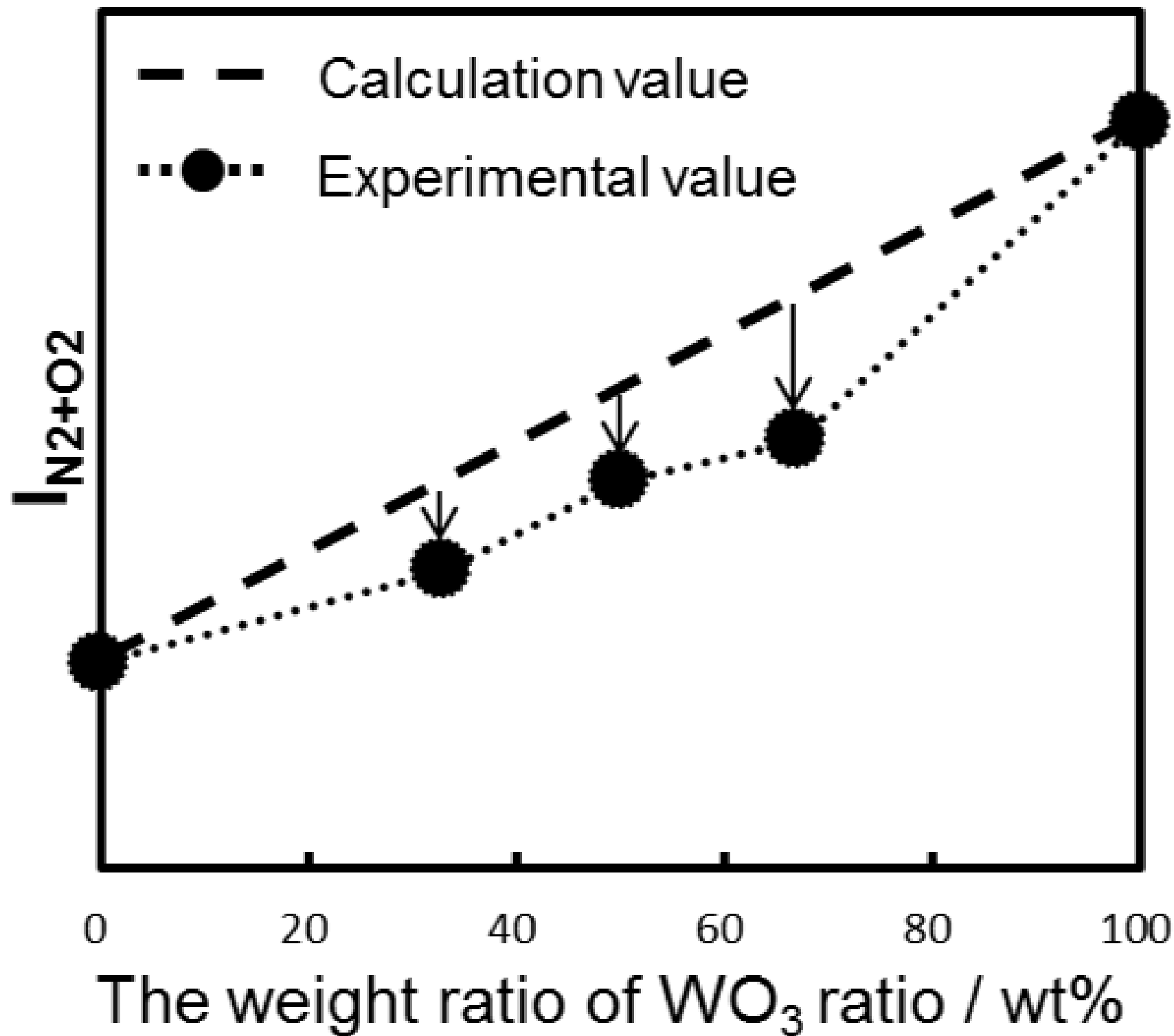
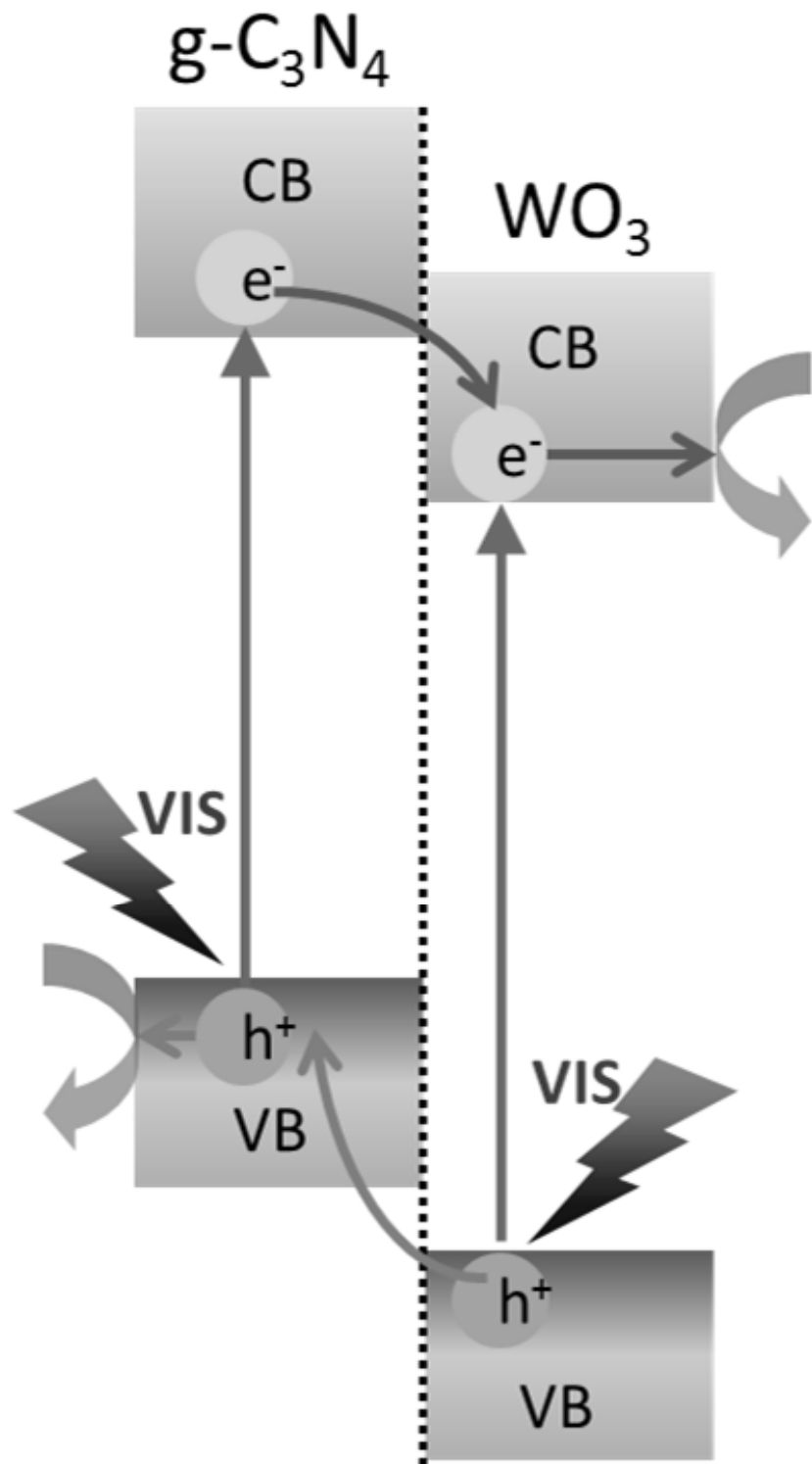




Fig. 10

(a)



(b)

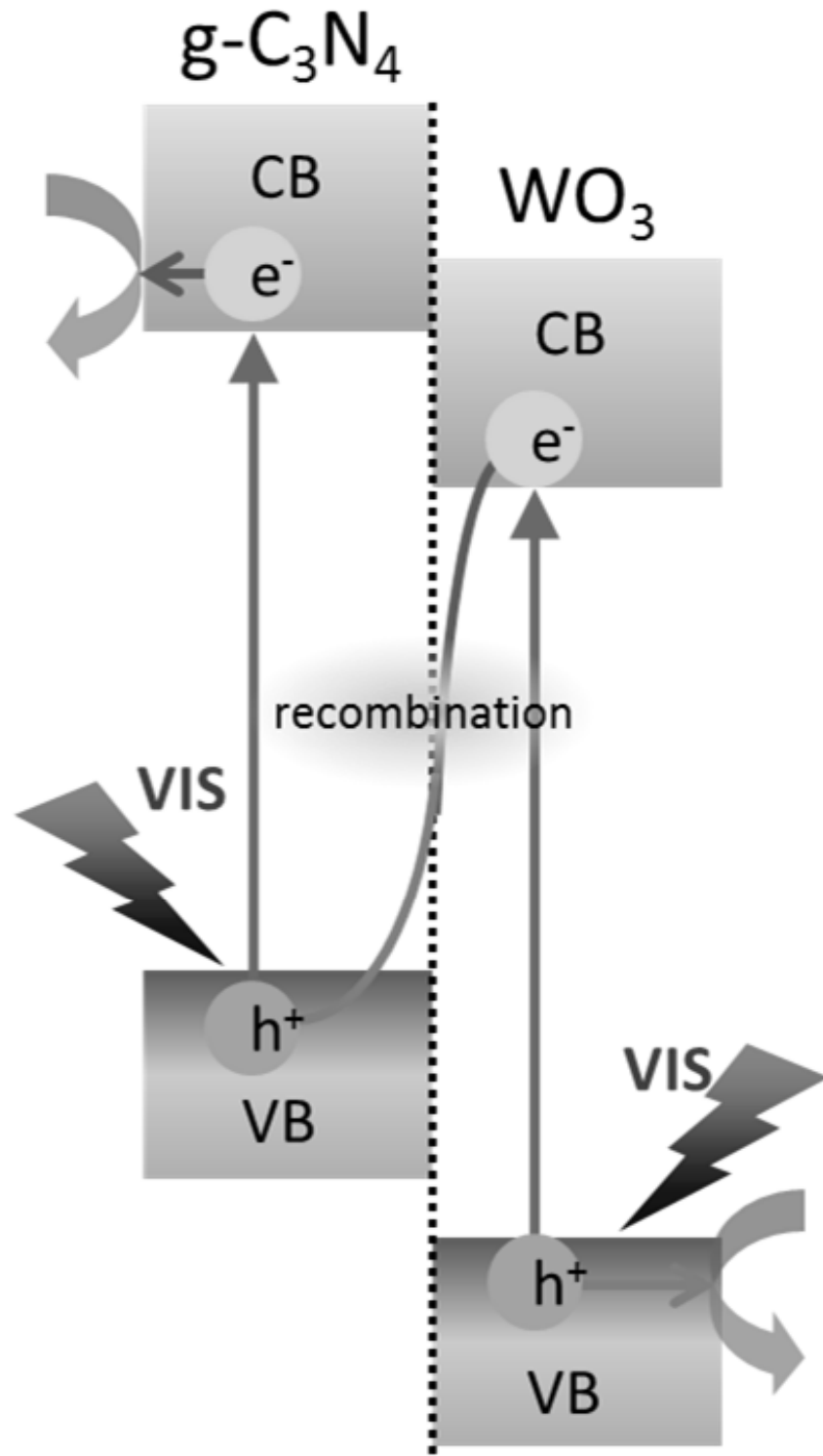
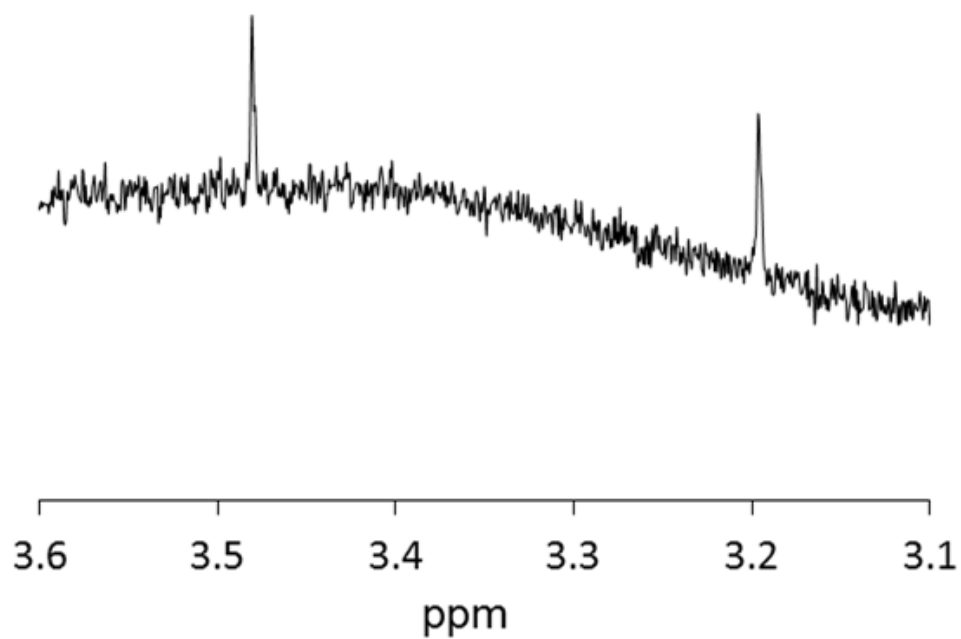
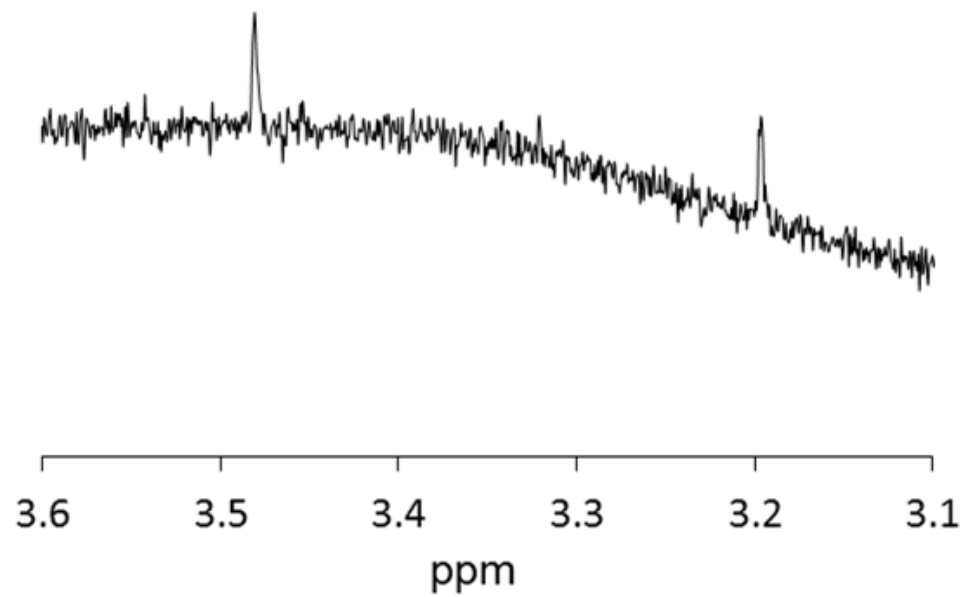


Fig. 11

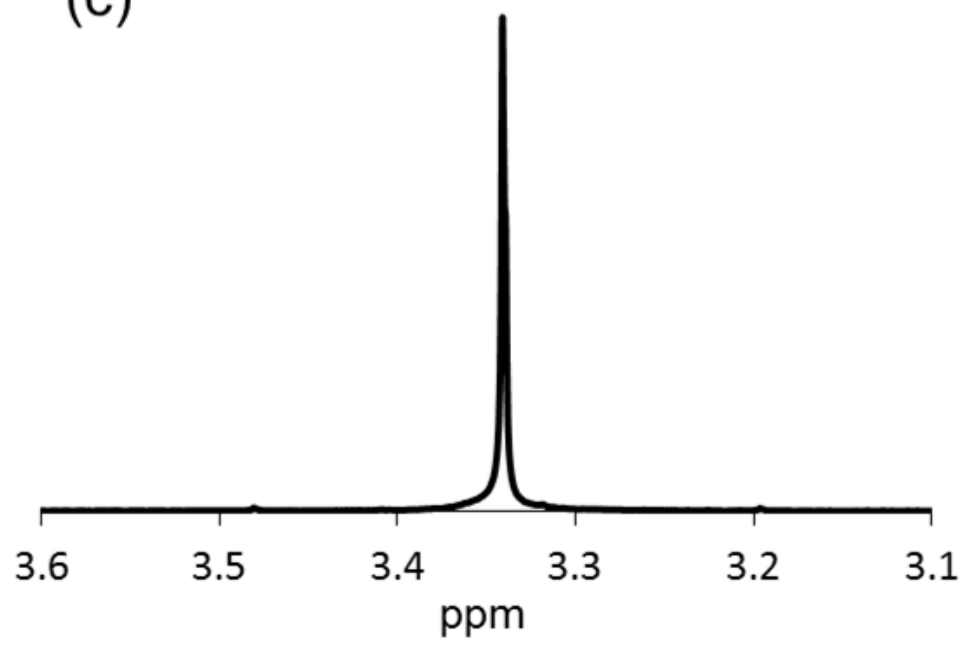
(a)



(b)



(c)



(d)

